Journal Name

Correlation between *in-situ* structural and optical characterizations of the semiconductor-to-metal phase transition of VO$_2$ thin films on sapphire

Tiziana Cesca,[*a] Carlo Scian,[a] Emilija Petronijevic,[b] Grigore Leahu,[b] Roberto Li Voti,[b] Gianmario Cesarini,[b,c] Roberto Macaluso,[d] Mauro Mosca,[d] Concita Sibilia,[b] and Giovanni Mattei[*a]

A detailed structural investigation of the semiconductor-to-metal transition (SMT) in vanadium dioxide thin films deposited on sapphire substrates by pulsed laser deposition was performed by *in-situ* temperature-dependent X-ray diffraction (XRD) measurements. The structural results are correlated with those of infrared radiometry measurements in the SWIR (2.5-5 μm) and LWIR (8-12 μm) spectral ranges. The main results indicate a good agreement between XRD and optical analysis, therefore demonstrating that the structural transition from monoclinic to tetragonal phases is the dominating mechanism for controlling the global properties of the SMT transition. The picture that emerges is a SMT transition in which the two phases (monoclinic and tetragonal) coexist during the transition. Finally, the thermal hysteresis, measured for thin films with different thickness, showed a clear dependence of the transition temperature and the width of the hysteresis loop on film thickness and on the size of the crystallites.

1   Introduction

The capability to engineer and modulate the material properties at the nanoscale through the control of some external parameters is a key issue for the development of advanced, tunable nanophotonic devices.[1,2] Within this framework, very interesting opportunities are offered by phase-change materials (PCMs) owing to the large changes of electrical and optical properties that occur in these materials upon their phase transition.[3–5]

Among the PCMs, vanadium dioxide (VO$_2$) is definitely one of the most promising materials and is finding application in a continuously growing number of different fields.[6–13] Discovered for the first time by Morin in 1959,[14] VO$_2$ is characterized by a reversible, first-order semiconductor-to-metal phase transition (SMT), which occurs right above room temperature (at about 68 °C). Upon the SMT, the material switches from the semiconductor state (with a monoclinic crystallographic structure) to the metallic state (tetragonal, rutile structure), changing drastically its electrical properties (electrical conductivity may change up to

five orders of magnitude[15,16]) as well as the optical[17] and infrared properties[18,19] (i.e. reflectance and emissivity). The VO$_2$ phase transition can be induced thermally, but also electrically and optically,[20–23] making VO$_2$ thin films of great interest for the realization of ultra-fast optical switches and modulators.[24,25]

The change of physical properties in vanadium dioxide during the phase transition is also characterized by an hysteresis loop whose temperature width varies from few degrees (2-3 °C) in single crystals, up to few tens of degrees (10-40 °C) in thin films containing small nanocrystals with different sizes.[26–31] The possibility to control the hysteresis parameters and the SMT properties by choosing specific technologies for the thin film deposition is very important for many applications, as for example for heat management[32,33] or thermal camouflage,[34–39] and thus much work has been devoted to the study of VO$_2$ thin films realized with different methods, such as reactive evaporation,[40] sputtering,[41–44] metal-organic-chemical-vapor deposition (MOCVD),[45,46] sol-gel deposition[47] and pulsed laser deposition (PLD).[48,49]

In spite of the wide investigation performed in the last years on the optical and electrical properties of VO$_2$ thin films upon the phase transition and the structural characterization of the initial and final states of the STM, much less is known about the kinetics of the structural processes occurring during the SMT. In 2010 Yao et al. performed an *in-situ* investigation of single-crystalline VO$_2$ by temperature-dependent X-ray absorption fine structure (XAS)

^{a} *University of Padova, Department of Physics and Astronomy, NanoStructures Group, via Marzolo 8, I-35131 Padova, Italy. E-mail: tiziana.cesca@unipd.it, giovanni.mattei@unipd.it*

^{b} *Department SBAI, Sapienza University of Roma, Via A. Scarpa 14, I-00161 Rome, Italy*

^{c} *INFN, Sezione di Roma, Piazzale Aldo Moro 2, I-00185 Rome, Italy*

^{d} *Department DEIM, University of Palermo, Viale delle Scienze, I-90128 Palermo, Italy*

measurements and compared the results with electrical measurements, suggesting a cooperative mechanism between a structure-driven Peierls transition and an electron-correlation driven Mott transition.[50] Nonetheless, a clear link between the nanoscale structural evolution across the SMT and the change of macroscopic optical and electrical properties of VO_2 thin films has not been found yet.

In the present work we report on the results of a structural characterization of the phase transition of VO_2 thin films deposited by pulsed laser deposition (PLD) on sapphire substrates obtained by *in-situ* X-ray diffraction (XRD) measurements as a function of temperature. The results are compared with those obtained with infrared radiometry measurements in the SWIR (2.5-5 μm) and LWIR (8-12 μm) range. PLD was chosen as deposition technique since it is one of the most inexpensive and convenient methods for growing VO_2 thin films with the highest contrast of their electric and optical properties across the metal-insulator transition.[51] Thin films with different thicknesses were deposited to determine also how the main parameters of the thermal hysteresis of the phase transition change with thickness and nanostructure.

2 Experimental

2.1 Samples fabrication

Vanadium dioxide thin films were realized by pulsed laser deposition (PLD) onto 2 cm x 2 cm sapphire substrates at the oxygen pressure of 10^{-2} mbar and temperature of 550 °C. Three VO_2 layers with different thicknesses were deposited: 135 nm (sample S1), 90 nm (sample S2) and 45 nm (sample S3). The PLD system employed is described in details elsewhere[52,53]. It uses a Q-switched tripled Nd:YAG laser (Quantel mod. YG78C20, λ=355 nm) generating 6 ns width pulses with energy of 80 mJ/pulse. The density of energy was maintained at 1.2 J/cm^2, and the repetition rate was 20 Hz. The VO_2 target was a 15 mm diameter, 5 mm-thick disk obtained by VO_2 powder cold pressing (purity 99.9%, Sigma Aldrich). Before each deposition, the substrates were cleaned in an ultrasonic bath with acetone, subsequently rinsed with isopropanol and then dried up with compressed air. After cleaning, each substrate was clamped onto an electrical heater, which allowed to achieve temperatures as high as 600 °C. The heater was then placed inside a vacuum bell jar where oxygen gas can be introduced through an electromechanical valve to maintain the desired pressure. After the deposition, the films thickness was assessed by Rutherford backscattering spectrometry (RBS) and double-checked by profilometry.

2.2 Structural characterizations

The surface morphology of the VO_2 thin films was characterized by scanning electron microscopy (SEM) and atomic force microscopy (AFM) measurements. SEM measurements were carried out using a field-emission scanning electron microscope (FE-SEM, Zeiss Sigma HD) operating in the 0.2-30 kV range, while AFM characterizations were performed in non-contact mode with a NT-MDT (Solver-PRO) atomic force microscope.

X-ray diffraction (XRD) measurements were performed at room temperature to evaluate the crystalline structure of the deposited layers, and as a function of the temperature to directly follow the structural transition of the VO_2 phase and its thermal hysteresis in the samples. XRD scans were taken in grazing incidence (GIXRD, with grazing angle $\omega = 0.5$ deg) and $\omega - 2\theta$ geometry with a Panalytical X'Pert Pro high-resolution diffractometer working in parallel beam geometry with a CuK$_\alpha$ source. The system is equipped with an Anton Paar DHS900 heatable specimen holder for *in-situ* X-ray diffraction as a function of the temperature in the range 40-100 °C to achieve full SMT in both heating and cooling cycles taking into account possible hysteresis. For the *in-situ* measurements, ambient air atmosphere was used and the temperature was varied in steps of 2°C with heating (cooling) rate of 0.4°C/min and waiting about 5 minutes at each temperature to achieve thermalization before starting the X-ray measurements. The temperature was monitored by the thermocouple of the DHS900 setup mounted in close proximity to the back of the sample under investigation. An external calibrated PT100 thermoresistance in direct contact with the sample surface was used to monitor possible differences in the nominal temperature of the DHS900 with respect to the actual temperature at the sample surface (where the thin VO_2 layer is deposited). We verified that the temperatures were in perfect agreement, ruling out possible differences due to the thermal isolation of the sapphire substrate. We also checked out that no sample re-alignment was needed at each temperature due to thermal expansion of the samples.

2.3 Optical characterizations

The thermal transition of the samples was investigated by reflectance and transmittance measurements in the SWIR (2.5-5 μm) and LWIR (8-12 μm) infrared range (a scheme of the experimental set-ups is shown in ref.[18]). In both set-ups the same globar lamp is used as a source of infrared radiation. The lamp is kept at a temperature of about 130 °C through a stabilized power supply. The infrared radiation is modulated by a mechanical chopper before reaching the sample under test, and the same frequency is used for the external reference of the lock-in amplifier that provides data acquisition. For transmittance measurements, the IR radiation impinges on the sample at normal incidence, passes through the cylindrical central hole of the sample holder (10 mm in diameter), and is eventually collected by a Ge lens and detected by a (HgCdZn)Te photovoltaic IR sensor. For reflectance measurements, the IR radiation is sent to the sample at near-normal incidence, is then reflected back and eventually detected by the same detection system.[18,38,39] Two different kinds of (HgCdZn)Te photovoltaic IR detectors have been used. For the analysis in the SWIR range the Vigo System model PVI-5 detector has been chosen due to the high sensitivity in the range (2.5-5.0 μm). For the analysis in the LWIR range the Vigo System model PVI-4TE-10.6 detector has been selected due to the flat responsivity in the wide range (3-12 μm). In this case the detector has been coupled with a long pass filter with transmission of 90% in the LWIR (8-12 μm) range so to obtain a narrow band. The sample is placed on an electrical heater to perform a temperature scan from 30 °C to 100 °C so to analyze the vanadium dioxide phase transition. The temperature of the sample
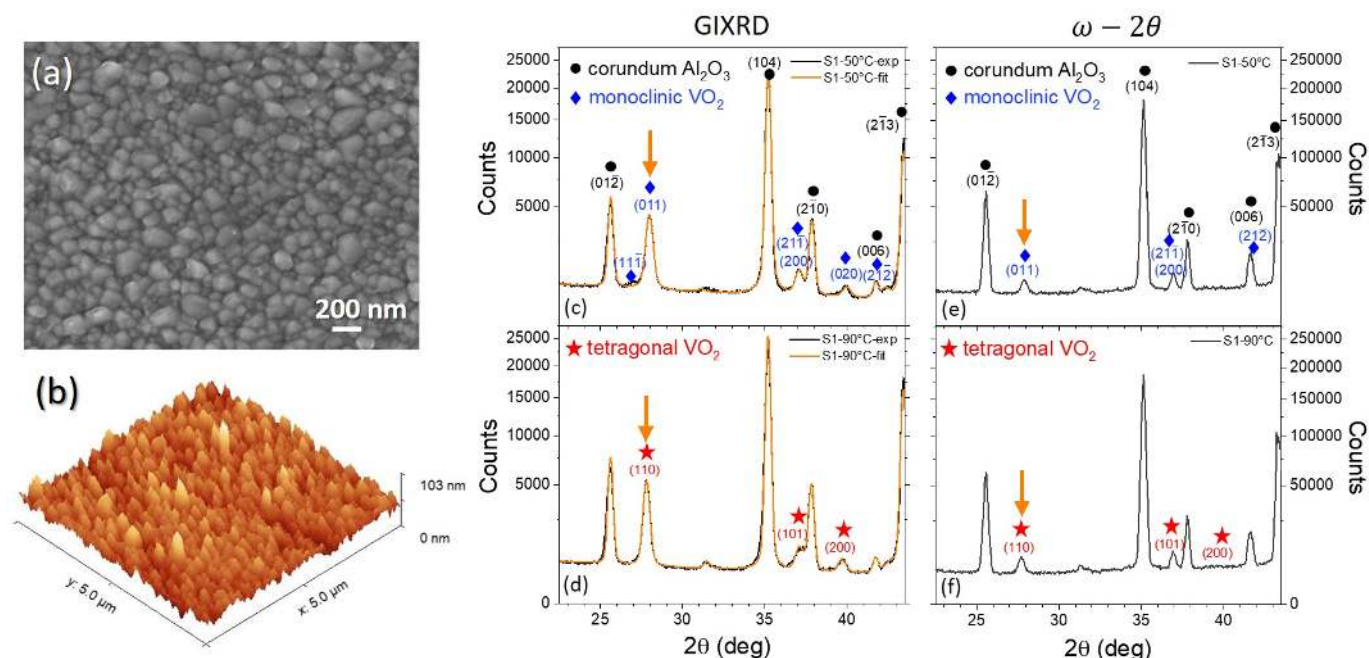
Fig. 1 (a) SEM image in plane view and (b) 3D AFM image of sample S1 ($t_{VO_2} = 135$ nm). (c,d) GIXRD patterns of sample S1 taken at (c) T = 50 °C and (d) T = 90 °C; the diffraction peaks of monoclinic (M_1) VO$_2$ (blue), tetragonal (rutile R) VO$_2$ (red) and the corundum Al$_2$O$_3$ substrate (black) are indicated. The orange solid line is the best fit to the experimental data. (e,f) $\omega - 2\theta$ patterns of sample S1 taken at (e) T = 50 °C and (f) T = 90 °C (red). The orange arrow marks the (110) VO$_2$ diffraction peak whose position was followed as a function of the temperature during the phase transition.

is measured by a copper-constantan thermocouple, and, due to the low sample heat capacity, thin electrical wires of 0.05 mm in diameter (type TG-40-T, NY Thermoelectric Co., Inc.) were used to minimize the heat losses from the contact points of the thermocouple. The temperature scan of the sample is performed in a quasi-stationary regime, realized by changing linearly the sample temperature slowly with time, with a low speed of about 1 °C/min.

3   Results and discussion

3.1   Structural properties of VO$_2$ thin films on sapphire

The surface morphology of the VO$_2$ layers obtained by pulsed laser deposition is characterized by the presence of interconnected, spherical grains of different sizes in the range 10-200 nm. As an example, fig. 1 shows a SEM image in plane view (a) and a 3D AFM image (b) of sample S1 (thickest VO$_2$ layer, $t_{VO_2} = 135$ nm). The mean surface roughness was determined by the analysis of the AFM images and results of about 7 nm. In fig. 1(c-f) we reported the XRD patterns of sample S1 obtained in (c,d) GIXRD and (e,f) $\omega - 2\theta$ configuration, measured at T = 50 °C (upper panels) and T = 90 °C (lower panels). At low temperature, fig. 1(c,e), the patterns show the diffraction peaks of both the corundum Al$_2$O$_3$ substrate (black) and the VO$_2$ film in the monoclinic phase (blue), corresponding to its semiconductor state. Structural refinement with Maud software [54] of the monoclinic phase ($P2_1/c$, M_1 phase) resulted in the following parameters: $a_{M_1} = 0.575(1)$ nm, $b_{M_1} = 0.452(1)$ nm, $c_{M_1} = 0.536(1)$ nm and $\beta_{M_1} = 122.8(2)$ deg, which is in good agreement with the literature data [55]. At high temperature, as shown in fig. 1(d,f), it is pos-

sible to observe the transition of VO$_2$ from monoclinic to rutile phase (red), corresponding to its metallic state. Structural refinement for the rutile (tetragonal) phase ($P4_2/mnm$, R phase) gave $a_R = b_R = 0.4532(2)$ nm, $c_R = 0.2873(3)$ nm, in good agreement with literature data as well, satisfying the rule $a_{M_1} = 2c_R$, [22,31] expected for the dimerization of the $V - V$ distance along the c_R axis on going from R to M_1, with the consequent doubling of the unit cell. No other vanadium oxide crystalline phases different from VO$_2$ have been evidenced. Moreover, a comparison of the GIXRD and $\omega - 2\theta$ measurements was done to evaluate the approximate shape of the nanocrystalline domains of VO$_2$. Indeed, they exhibit similar size in the perpendicular direction with respect to the sample surface (probed by the $\omega - 2\theta$ scan) with respect to the parallel one (probed by the GIXRD scan): for instance in the S1 sample the Scherrer analysis on the full width at half maximum (FWHM) of the (110) peak of the monoclinic (M_1) phase resulted in a $FWHM_{GIXRD}^{M_1} = 0.465$ deg and $FWHM_{\omega-2\theta}^{M_1} = 0.450$ deg, which correspond (considering the instrumental broadening) to a size of about $D_{\parallel}^{M_1} = 22$ nm and $D_{\perp}^{M_1} = 23$ nm, respectively. In the same sample the high-temperature (110) R phase has a $FWHM_{GIXRD}^{R} = 0.420$ deg and $FWHM_{\omega-2\theta}^{R} = 0.405$ deg, which correspond to a size of about $D_{\parallel}^{R} = 25$ nm and $D_{\perp}^{R} = 26$ nm, respectively, which can be consistent with the rearrangement of the unit cell (considering the doubling of the unit cell upon SMT, we found a 3% expansion of the structure). Similar results are also obtained for the S2 and S3 samples. Therefore, within the accuracy of the Scherrer technique we can consider the VO$_2$ nanograins as spherical, and in the following we used the GIXRD scans for the hysteresis analysis due to their inherent better sen-
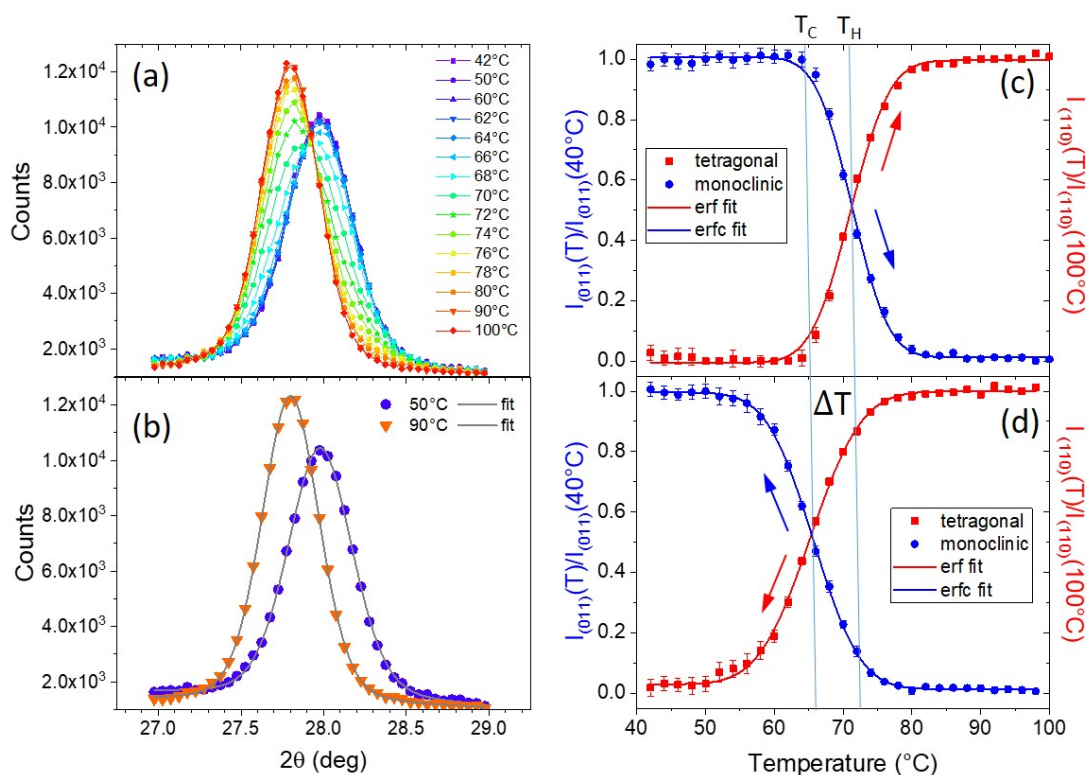
Fig. 2 GIXRD scans as a function of temperature of sample S1: (a) close-up view around the VO$_2$ (110) peak at different temperatures during a heating cycle; (b) examples of peaks fits according to the Voigt function (gray solid lines); (c) evolution of the normalized (110) peak intensity of the GIXRD scan in the S1 sample upon heating and (d) cooling as a function of temperature. Solid lines are fit to the experimental data with the *erfc* (blu lines) and *erf* (red lines) functions.

sitivity to surface layers with respect to the $\omega - 2\theta$ ones. In order to get deeper insights on the semiconductor-to-metal transition of the VO$_2$ films from a structural point of view, we monitored the evolution of the VO$_2$ diffraction peaks, as a function of the sample temperature, using an *in-situ* technique which allows to acquire XRD measurements while the sample performs heating and cooling cycles at specific temperature steps. Particularly, to determine the thermal hysteresis cycles of the deposited samples, we followed the shift with the temperature of the VO$_2$ (110) peak (orange arrows in fig. 1(c-f)), which is the most intense one and well separated from the substrate peaks. As an example, in fig. 2(a) we reported the GIXRD scans of sample S1, in the angular region around the VO$_2$ (110) peak, measured at different temperatures in the range 40-100°C during a heating-up cycle of the sample. The progressive shift of the peak position from 27.975 deg to 27.798 deg can be clearly observed by increasing the sample temperature, which corresponds to the transition of the VO$_2$ layer from monoclinic M_1 (semiconductor) to tetragonal R (metallic) phase, respectively. Similarly, a peak shift in the reverse direction is observed during the cooling cycle (not shown). The asymptotic phases peaks were fitted with a pseudo-Voigt profile plus a linear background. As an example, fig. 2(b) shows the results of the fits (gray lines) for the two cases in which the sample is heated at 50 °C (violet dots) and 90 °C (orange triangles). At temperatures around the SMT transition, we analyzed the resulting peak

assuming first that it was as a combination of the two peaks of the monoclinic and tetragonal phases, which are supposed to co-exist during the transition. The resulting analysis for the sample S1 is reported in fig. 2(c,d), which shows the thermal evolution of the intensity of the (011) peak of the M_1 phase and of the (110) peak of the R phase, normalized to the respective asymptotic intensities. A comparison between fig. 2(c) and fig. 2(d) (heating and cooling cycle, respectively) clearly reveals the presence of an hysteresis in the transition, whose width is $\Delta T = T_H - T_C$, where T_H and T_C are the transition temperatures during the heating and cooling cycles, respectively. Of course, such kind of fit involves the use of two pseudo-Voigt functions, with four fitting parameters each (amplitude, mixing coefficient, two widths, the centroid being fixed to the asymptotic value found from the single-peak analysis of fig. 2(b)), together with a linear function for the background (two additional fitting paramenters, i.e., slope and intercept). Therefore, the total number of fitting parameters is $2 \times 4 + 2 = 10$. This could result in numerical instabilities of the fit. Therefore, to obtain a more robust fit and following the XAS interpretation of the SMT transition given in ref. [50], we decided to adopt a single-peak analysis of the SMT transition, in which the two phases undergo a continuous structural transformation. The results of the two adopted analysis techniques of the GIXRD spectra gave the same values of the T_H and T_C temperatures, within the experimental accuracy. Therefore we preferred the continu-
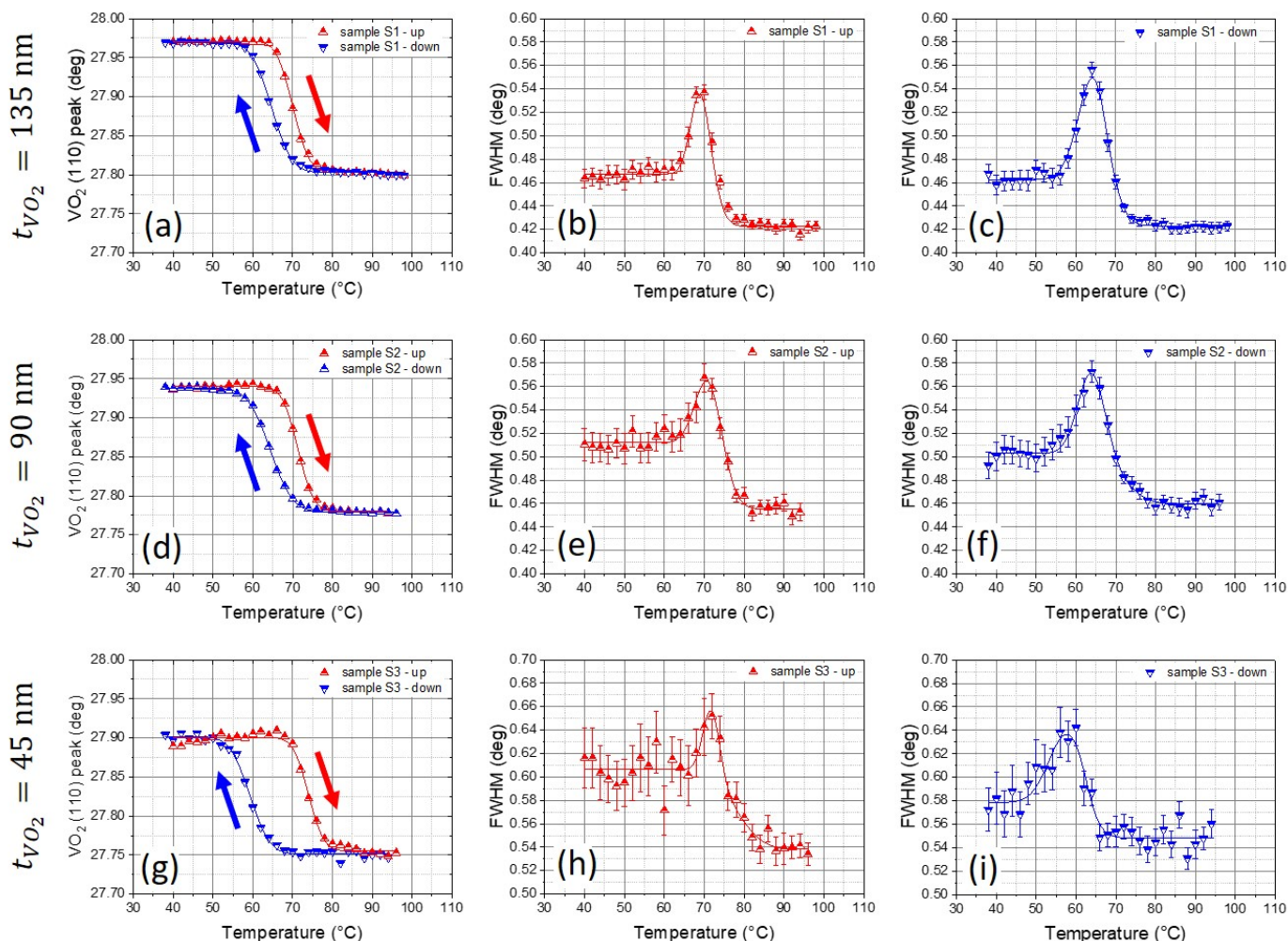
Fig. 3 Evolution of the VO$_2$ (110) GIXRD peak as a function of the sample's temperature for the three deposited samples: S1 (t$_{VO_2}$ = 135 nm, panels a-c), S2 (t$_{VO_2}$ = 90 nm, panels d-f), S3 (t$_{VO_2}$ = 45 nm, panels g-i). First column (panels a,d,g): VO$_2$ (110) peak position vs temperature during the heating (red symbols) and cooling (blue symbols) cycles. Second and third column: FWHM of the VO$_2$ (110) peak vs temperature during the heating (red symbols) and cooling (blue symbols) cycles.

ous phase transition analysis mode for its intrinsic higher numerical stability. In order to precisely determine the peak position and its width at each temperature step, we developed an automatic peak fitting procedure using one pseudo-Voigt peak function and a linear function for the background (6 fitting parameters). The results of this analysis are displayed in fig. 3(a-i) for all the three samples S1 (t$_{VO_2}$ = 135 nm), S2 (t$_{VO_2}$ = 90 nm) and S3 (t$_{VO_2}$ = 45 nm). In the first column, the graphs show the VO$_2$ (110) peak position as a function of the sample's temperature, during the heating (red symbols) and cooling (blue symbols) cycles. A clear hysteresis in the peak position as a function of the temperature can be observed for all the three samples (fig. 3(a,d,g)), whose width progressively increases by reducing the thickness of the VO$_2$ layer. In order to determine the transition temperatures during the heating and cooling cycles (T_H and T_C) and the width of the thermal hysteresis ($\Delta T = T_H - T_C$), we fitted the data of the peak position vs temperature with the *complementary error function (erfc)*,

according to the equation:

$$f(T) = \left(\frac{f_l + f_h}{2} \right) + \left(\frac{f_l - f_h}{2} \right) erfc \left[\frac{\sqrt{2}(T - T_0)}{\sigma} \right] \quad (1)$$

where f_l and f_h are the asymptotic values of the function in the low (f_l) and high (f_h) temperature ranges, and T_0 is the temperature at the inflection point (i.e., at which the function $f(T)$ reaches 50% of its change), corresponding to T_H or T_C for the heating or cooling cycles, respectively. The parameter σ is related to the width of the temperature interval around the T_0 temperature at which the transition occurs. The solid lines in fig. 3(a,d,g) are the best fits obtained with equation 1. The thermal hysteresis parameters determined from the fits of the three samples (S1, S2 and S3) are summarized in Table 1. It is worth noting that the transition temperature T_H is always higher than the expected value of 68 °C, independently of the sample (S1, S2, S3). A possible explanation of this behavior is that the crystallographic orientation of VO$_2$ depends strongly on the substrate, producing

Table 1 Thermal hysteresis parameters of the three samples (S1, S2 and S3) obtained from GIXRD measurements and optical characterizations in the SWIR (transmittance T and reflectance R) and LWIR (reflectance R) wavelength range; in the LWIR range, transmittance through the 0.5 mm sapphire substrate is negligible (T=0.001). The transition temperatures during the heating and cooling cycles (T_H and T_C) are calculated from the fits of the data using eq. 1; $\Delta T = T_H - T_C$ is the width of the thermal hysteresis.

| | Sample S1 $t_{VO_2} = 135$ nm | | | | Sample S2 $t_{VO_2} = 90$ nm | | | | Sample S3 $t_{VO_2} = 45$ nm | | | |
| | GIXRD | SWIR (2.5-5 μm) | | LWIR (8-12 μm) | GIXRD | SWIR (2.5-5 μm) | | LWIR (8-12 μm) | GIXRD | SWIR (2.5-5 μm) | | LWIR (8-12 μm) |
(°C)		T	R	R		T	R	R		T	R	R
T_H	70.0 ±0.1	70.5 ±0.1	73.1 ±0.1	74.9 ±0.2	71.3 ±0.1	71.9 ±0.2	73.5 ±0.1	76.6 ±0.2	73.9 ±0.2	75.1 ±0.2	75.3 ±0.1	80.1 ±0.5
σ_H	6.6 ±0.2	7.1 ±0.3	9.2 ±0.4	7.8 ±0.5	6.3 ±0.2	7.8 ±0.4	9.0 ±0.4	8.0 ±0.7	6.1 ±0.6	9.1 ±0.5	8.5 ±0.4	7.3 ±1.3
T_C	64.7 ±0.1	63.8 ±0.2	66.4 ±0.2	68.4 ±0.2	65.4 ±0.1	63.3 ±0.2	65.8 ±0.2	68.9 ±0.2	59.3 ±0.2	62.8 ±0.2	63.2 ±0.2	68.7 ±0.5
σ_C	8.0 ±0.2	7.7 ±0.5	10.4 ±0.5	9.4 ±0.6	8.8 ±0.2	9.4 ±0.5	11.1 ±0.5	9.7 ±0.6	8.0 ±0.5	10.0 ±0.6	9.3 ±0.5	9.0 ±1.3
ΔT	5.3 ±0.2	6.8 ±0.3	6.7 ±0.3	6.5 ±0.4	7.0 ±0.2	8.6 ±0.4	7.7 ±0.3	7.8 ±0.4	14.6 ±0.4	12.2 ±0.4	12.1 ±0.3	11.4 ±1.0
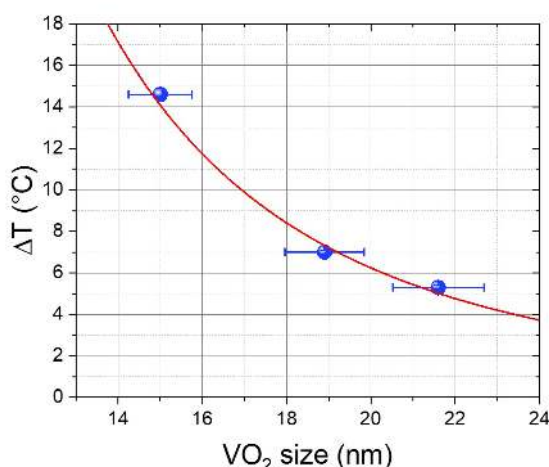
Fig. 4 Evolution of hysteresis width ΔT as a function of the average diameter of the room temperature monoclinic VO$_2$ crystallites. The solid line is a fit to the experimental data with the size-equation $\Delta T(D) = A/D^\alpha$.
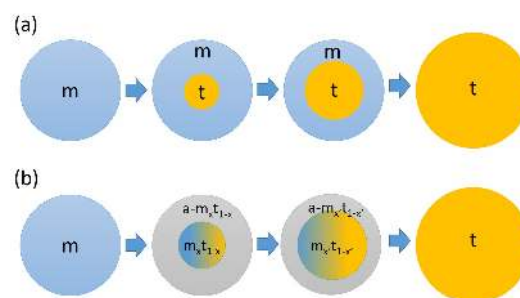

Fig. 5 Sketch of the possible crystalline phases during the heating cycle for a single VO$_2$ crystallite: (a) during the SMT transition, the monoclinic (m) and tetragonal (t) phases coexist (a core-shell or a segregated arrangement could be adopted) or (b) continuous phase transformation, in which a crystalline core domain of the inter-phase $m_x t_{1-x}$ is surrounded by a more disordered (amorphous-like) inter-phase, a-$m_x t_{1-x}$, which is not detectable in the GIXRD measurement.

different strains in the layers, which affect the phase transition temperatures. For example for m- and r-plane sapphire substrates, VO$_2$ appears to transform abruptly from the monoclinic phase to the rutile structure as the temperature is increased, while VO$_2$ deposited on c-plane sapphire exhibits a sluggish transformation. For these three cases, Nazari et al.[56–58] found different values of the transition temperature by ellipsometry: 72±2 °C, 63±2 °C, and 62±2 °C for c-, m-, and r-plane sapphire substrate, respectively. Moreover, an increase of T_H is always found because of strain and defects due to either the lattice mismatch between film and substrate or for hydrostatic pressure on the crystallites.[31] Therefore since interfacial phenomena become dominant as the film thickness decreases, T_H results higher for the thinnest sample S3 than for the thicker ones S2 and S1 (see Table 1). The width of the thermal hysteresis, $\Delta T = T_H - T_C$, is related to the size of the VO$_2$ crystallites formed during the deposition process and the presence of grain boundaries.[31] Many articles show that the width of the hysteresis loop increases by decreasing the do-

main size of the VO$_2$ crystallites.[26–30,59,60] Moreover, in thin films an enlargement of the hysteresis loop is observed due to the size poly-dispersion of the crystallites and the presence of a high density of large-angle, randomly oriented grain boundaries. Within this framework, the observed progressive increase of the thermal hysteresis width with decreasing of the thickness of the VO$_2$ layer can be related to the formation of VO$_2$ crystallites with smaller, randomly oriented domains. Fig. 4 shows the evolution of the hysteresis width ΔT as a function of the VO$_2$ monoclinic crystallite size obtained from the Scherrer analysis of the (011) diffraction peak width. The solid line is a nonlinear fit of the experimental data with the size-equation $\Delta T(D) = A/D^\alpha$, where D is the average diameter of the room temperature monoclinic VO$_2$ crystallites (zero hysteresis is assumed for infinitely large crystallites). The best fit parameter is $\alpha = 2.9 \pm 0.3$, thus indicating that, in our system, ΔT is roughly inversely proportional to the crystallite volume.

The transition width, σ, is determined too by the presence of defects (point defects, impurities, clusters) and the grain boundary area, and it is directly proportional to the overall defect density. In the present case, no significant difference is observed

as a function of the film thickness; conversely, for all the three samples, the parameter σ results always smaller for the heating cycles than for the cooling ones ($\sigma_H < \sigma_C$), demonstrating that the hysteresis is asymmetrical, as also found in ref.[18]. We can ascribe this asymmetry to a different strain contribution during heating and cooling cycle related to the interplay among three factors: (i) the variation of the volumetric density upon SMT, (ii) the size distribution of the VO_2 crystalline domains and (iii) the strain controlled by the amorphous/defective phases (the 'matrix') in the system. Likely, when the M_1 crystals are heated, their size distribution will produce a distribution of transition temperatures to the R phase, the lower ones being likely related to the largest/defect-free crystallites, and the progressively larger ones to smaller/defective crystallites. The width of this distribution is σ_H and it is slightly 'compressed' toward higher temperature values by the pressure exerted by the 'matrix' on the size-distributed crystallites. After the SMT transition is completed and the cooling cycle is started, considering that M_1 has a smaller volumetric density with respect to the R phase, the crystallites will relax easier to the M_1 phase since they exhibit a generally reduced interaction with the 'matrix'. This results in a broader transition temperature distribution (σ_C) with respect to the heating cycle, producing the observed asymmetry in the hysteresis loops.

The second and third columns of fig. 3 report the trend of the full width half maximum (FWHM) of the VO_2 (110) peak during the heating (red symbols) and cooling (blue symbols) cycles, respectively. The solid lines are best fits to the data, obtained combining a sigmoidal and a Gaussian function to be used as a guide for the eye. For each sample, the FWHM for the low temperature (monoclinic) phase is larger that the corresponding value for the tetragonal one, indicating a smaller crystallite size at low temperature. This is in agreement with the difference in the unit cell volume for the two phases. Moreover, the graphs show that the peak width reaches its maximum value at the transition temperatures (T_H and T_C). This result can be understood considering the single-peak analysis used: if one assumes that the two phases coexist at the transition (see fig. 5(a)), the peak width is expected to be larger because actually it represents two convoluted peaks whose centroids differ by much less than the peak widths. On the other hand, if we assume the continuous transition model[50], the larger peak width could be understood as the nucleation of a crystalline inter-phase coupled with an amorphous or disordered phase as in a core-shell-like structure, like in fig. 5(b). Moreover, progressively larger peak widths are measured in the sample with the decreasing VO_2 film thickness, indicating, according to the Scherrer equation, progressively smaller crystallite sizes for both the monoclinic and tetragonal phases as the sample thickness decreases (the higher level of noise for the S3 sample is a consequence of the lower signal of the VO_2 peak in this sample due to its small thickness). In order to collect additional data for determining which model better describes the SMT microscopic structure (i.e., cohexistance of the two phases or continuous phase transformation, as sketched in Fig. 5), we investigated the hysteretic behavior of the same sample with optical measurements (transmittance and reflectance) in the *IR* range which are not sensitive to the crystalline structure but to the global dielectric nature of the effective medium representing the VO_2 thin films.

3.2 Infrared properties of VO_2 thin films on sapphire

In this section we show the infrared radiometric measurements performed upon phase transition on the different VO_2 thin films deposited on the sapphire substrate. The analysis has been performed in both the SWIR range (2.5-5 μm) and LWIR range (8-12 μm) by using the equipments described in section 2.3.

3.2.1 Analysis in the SWIR range

The hysteretic behavior as a function of the temperature of both reflectance and transmittance in the SWIR range (2.5-5 μm) is shown in fig. 6, where the difference between the heating (red symbols) and cooling (blue symbols) cycles is evidenced. The measurements have been performed both on the samples with different VO_2 thickness and on the sapphire substrate taken as a reference; fig. 6 shows the results in the temperature range between 50 °C and 90 °C.

From a first inspection of fig. 6 it emerges that reflectance switches from the low value around 0.1 at 30 °C, when VO_2 is in the semiconductor state ($R = 0.09$ is for the sapphire substrate only), to larger values at 90 °C, when VO_2 is in the metallic state. Moreover, the metallic VO_2 film exhibits increasing reflecting properties with its thickness. On the other hand, upon phase transition, transmittance drastically decreases due to the strong absorption properties of VO_2 in the metallic state. In fact at 90 °C an increasing opacity of the samples is found as the film thickness increases. In table 2 we reported the values of reflectance (R) and transmittance (T) measured for the three samples S1 (t_{VO_2} = 135 nm), S2 (t_{VO_2} = 90 nm) and S3 (t_{VO_2} = 45 nm), before (at 30°C) and after (at 90°C) the VO_2 phase transition; the corresponding values of the bare 0.5 mm sapphire substrate are reported as a reference. Another property to be investigated in thermochromic materials is the temperature dependent emissivity that is of fundamental importance for thermal regulation and heat management as well as for infrared camouflage, tagging and identification, and many other applications. Emissivity is the ratio between the sample thermal radiation and the ideal Planck's black-body radiation at the same temperature, and can be easily calculated from the R and T experimental data in fig. 6 by using the formula $\varepsilon = 1 - R - T$ according to Kirchhoff's law. In table 2 we reported the emissivity values for the three VO_2 samples, and the sapphire substrate, calculated from the measurements of R and T at 30°C and 90°C. The whole trend of ε as a function of the temperature for the three samples is shown in fig. 6(g-i). For all the samples, the temperature-dependent emissivity in the SWIR range exhibits a positive differential thermal emittance (compare rows 5 and 6 in table 2). Furthermore, the *anomalous absorption* phenomenon is clearly visible for samples S2 and S1 looking at the maximum emissivity (0.52±0.01) during the phase transition for both heating and cooling cycles, whereas it is absent for sample S3, probably due to the lower film thickness and the larger film/substrate interface influence.[31] *Anomalous absorption* occurs in the phase transition when nanoscale inclusions of the metallic phase emerge in the surrounding insulating-phase VO_2, grow and connect in a percolation process, eventually leading to
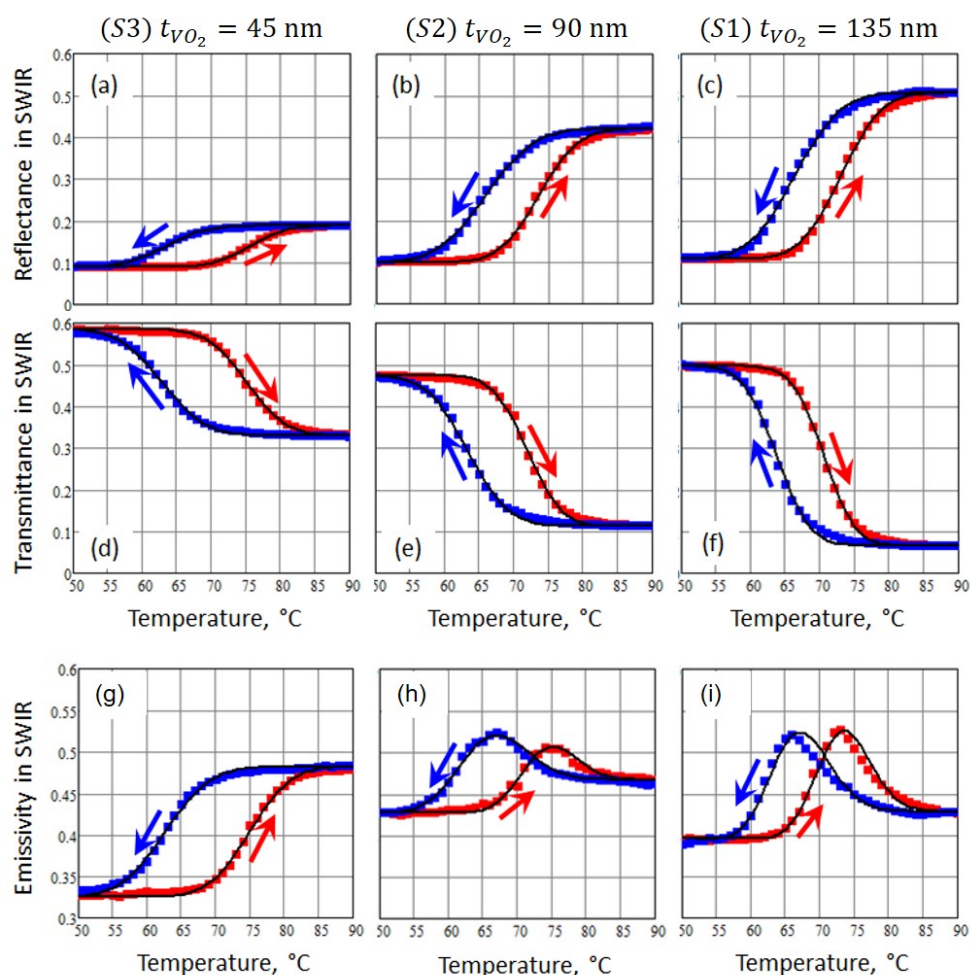
Fig. 6 IR reflectance, transmittance and emissivity *vs* temperature, in the range from 50-90 °C for the three VO$_2$ thin films deposited on sapphire. The measurements are performed in the SWIR (2.5-5 μm) range. Emissivity is calculated from the measurements of R and T by using the formula $\varepsilon = 1 - R - T$. Red (blue) color refer to the heating (cooling) cycle. The black continuous lines are the best fits obtained with equation 1 that simulates the thermal hysteresis. (a) Reflectance, (d) transmittance and (g) emissivity of sample S3 (t_{VO_2} = 45 nm); (b) reflectance, (e) transmittance and (h) emissivity of sample S2 (t_{VO_2} = 90 nm); (c) reflectance, (f) transmittance and (i) emissivity of sample S1 (t_{VO_2} = 135 nm).

a fully metallic state at the end of the transition. [18,32,34,35,61] This result seems to support the two phases coexistence model. Indeed, the Maxwell-Garnett model used to describe in the following analysis the film as an effective medium [18] is constructed by averaging over the filling fraction the dielectric functions of the two components, each of which with its own dielectric constants. Since metallic inclusions and film thickness are both much smaller than the light wavelength in the SWIR range, VO$_2$ behaves as a natural, reconfigurable, disordered metamaterial with tunable absorbance, showing an anomalous peak when VO$_2$ mixed phase and sapphire act as a lossy "ultra thin" resonator. [18,32,34,35] The thermal hysteresis parameters (T_H, T_C and $\Delta T = T_H - T_C$) have been calculated from the experimental data in fig. 6(a-f) using the same approach described in section 3.1. The black curves in fig. 6(a-f) are the best-fit results obtained with equation 1; the *error function* (*erf*) was used in this case. The fitting results are reported in table 1. For all the parameters, the values determined by the analysis of the radiometric curves are in agreement with the results obtained from the GIXRD measurements. In particular,

T_H results higher with respect to the expected value of 68°C for all the three samples and the width of the hysteresis loop increases by decreasing the sample's thickness, as observed for GIXRD measurements. Moreover, the sharpness of the transition for the heating cycles of the three samples is always smaller than for the corresponding cooling cycles ($\sigma_H < \sigma_C$), confirming the asymmetry of the hysteresis previously highlighted from the diffraction measurements. The small quantitative differences in the measured quantities may be due to the fact that GIXRD is sensitive to the crystalline phases only, whereas optical measurements take into account also the contribution of possible amorphous phases in the films. In any case, the obtained results confirm that the optical properties of the samples are mainly controlled by the structural evolution occurring to the crystalline phases during the thermal transition. To verify this point we have analysed the width of the hysteresis cycles ΔT measured by reflectance as a function of the VO$_2$ crystallite size obtained from GIXRD analysis. The results are shown in fig. 8. We used the same coefficient α=2.9 obtained from GIXRD analysis in the generalized size-equation

Table 2 Reflectance (R), transmittance (T) and emissivity (ε) values in the SWIR and LWIR ranges of samples S1, S2 and S3, before (at 30°C) and after (at 90°C) the VO$_2$ phase transition; transmittance in the LWIR range is $T = 0.001$ and has been neglected here. The values for the 0.5 mm sapphire substrate are also reported as a reference.

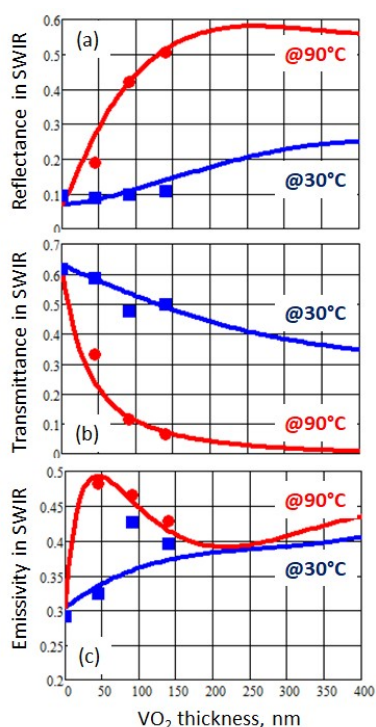|			Sample S1 (t_{VO_2} = 135 nm)	Sample S2 (t_{VO_2} = 90 nm)	Sample S3 (t_{VO_2} = 45 nm)	Sapphire (0.5 mm)
SWIR	**R**	30°C	0.11	0.10	0.09	0.09
		90°C	0.51	0.42	0.19	0.09
	T	30°C	0.50	0.47	0.59	0.62
		90°C	0.07	0.11	0.33	0.62
	ε	30°C	0.40	0.43	0.32	0.29
		90°C	0.43	0.47	0.48	0.29
LWIR	**R**	30°C	0.07	0.07	0.07	0.07
		90°C	0.48	0.35	0.09	0.07
	ε	30°C	0.93	0.93	0.93	0.93
		90°C	0.52	0.65	0.91	0.93

Fig. 7 (a) Reflectance, (b) transmittance and (c) calculated emissivity in the SWIR range (2.5-5 μm) vs VO$_2$ film thickness. Red (blue) colors are for the metallic (semiconductor) phase. Symbols are for the experimental results of samples S1 (135 nm), S2 (90 nm) and S3 (45 nm) and the bare sapphire substrate. Continuous lines are for the numerical simulations (see text for explanation).

Fig. 8 Evolution of hysteresis width ΔT obtained from reflectance measurements as a function of the average diameter of the room temperature monoclinic VO$_2$ crystallites. The solid line is a fit to the experimental data with the size-equation $\Delta T(D) = \Delta T(\infty) + A/D^{\alpha}$ assuming α = 2.9 as obtained from GIXRD.

$\Delta T(D) = \Delta T(\infty) + A/D^{\alpha}$ in which we have added the asymptotic term $\Delta T(\infty)$ to account for additional defect contributions of the amorphous phases not present in the GIXRD data. The obtained curve nicely fits the reflectance data (very similar to the transmittance ones), therefore further confirming the agreement between optical and structural analyses, even considering their sensitivity to different contributions in the samples.

From a quantitative analysis of both infrared reflectance and transmittance data shown in table 2 for the three samples S1, S2, S3 and for the 0.5 mm thick sapphire substrate, we estimated the vanadium dioxide effective refractive index as unique fit parameter for S1, S2 and S3, constant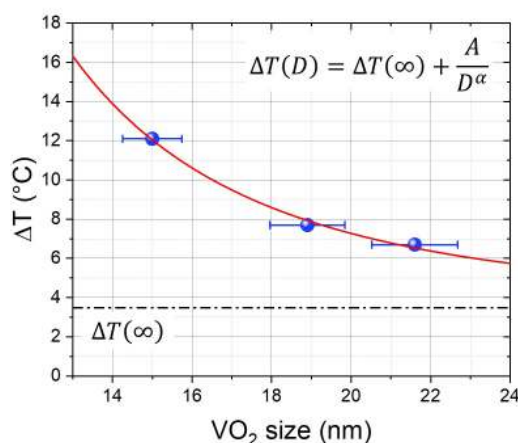 in the SWIR range. The effective value is determined from the best fit procedure between the data in table 2 and the numerical simulations where the possible VO$_2$ refractive indexes n are sampled among 5000 values in the range $2 < Re(n) < 4$ and $0 < Im(n) < 5$ (a sharp VO$_2$/sapphire interface has been assumed,[18] and the reference literature value has been used for the sapphire substrate.[62]). The best fit allows to find $n_C = 2.3 + 0.2i$ in the semiconductor phase, and $n_H = 3.6 + 3.2i$ in the metallic phase (corresponding to the minimum error respectively of 1.5% and 0.5%). Although n_C might seem a low value for vanadium dioxide, it is rather consistent with the wide range of values found in literature where VO$_2$ optical constants exhibit strong differences depending on the deposition technique,[20,63–71] the substrate temperatures[63] and the oxygen pressure[64] employed during the deposition process. Once all the optical properties are found, then IR reflectance, transmittance and emissivity of any VO$_2$/sapphire structure can be easily simulated and optimized as a function of VO$_2$ film thickness. The infrared properties of VO$_2$/sapphire structure vs the VO$_2$ film thickness are shown in fig. 7. Numerical simulations (continuous lines) have been carried out according to the following procedure: both transmittance
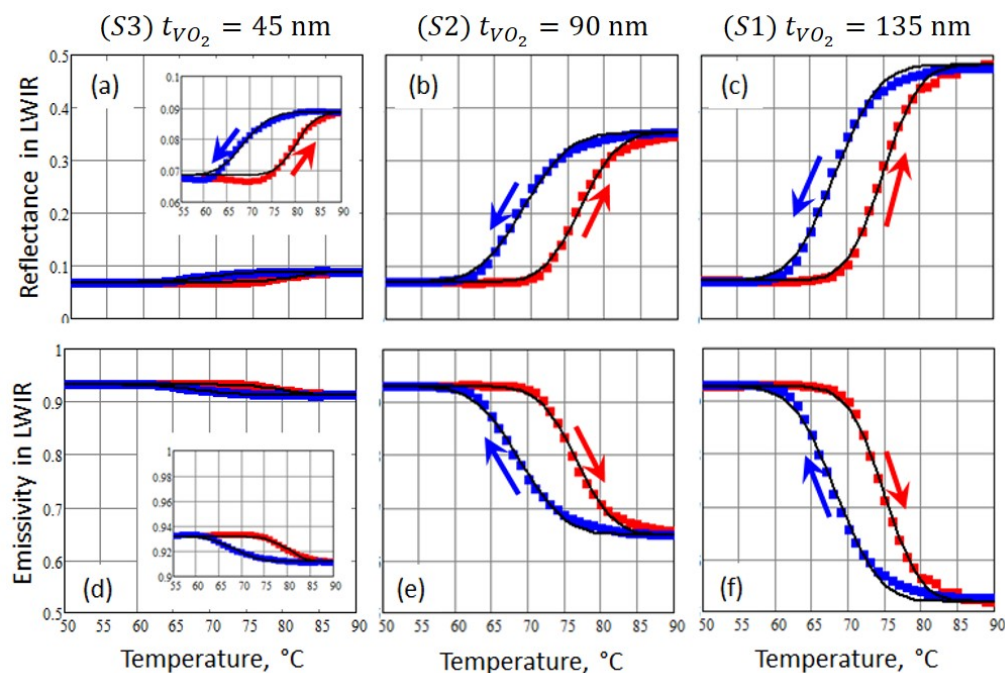
Fig. 9 Reflectance and emissivity *vs* temperature in the LWIR range (8-12 μm) for the three VO$_2$ thin films deposited on 0.5 mm sapphire substrate. Emissivity is calculated from the measurements of R by using the formula $\varepsilon = 1 - R$. Red (blue) colors are for the heating (cooling) cycles. Black continuous lines are for the best fit with equation 1. (a) Reflectance and (d) emissivity of sample S3 (45 nm); (b) reflectance and (e) emissivity of sample S2 (90 nm); (c) reflectance and (f) emissivity of sample S1 (135 nm). The insets in (a) and (d) are an enlargement of the corresponding plots along the vertical axis.

and reflectance spectra have been simulated by transfer matrix method for each VO$_2$ film thickness. Both spectra are weighted by the black-body Planck's radiation function at 130 °C, and finally averaged in the SWIR range. Averaged emissivity is calculated as $\varepsilon = 1 - R - T$. Simulations are in good agreement with the experimental measurements (symbols). They demonstrate also that both reflectance (fig. 7a) and transmittance (fig. 7b), after phase transition (at 90 °C), exhibit a strong dependence on the film thickness till 200 nm, while thicker films do not produce any substantial change. Analogously, the emissivity graph (fig. 7c) shows a positive differential emissivity ($\varepsilon_H - \varepsilon_C > 0$) only for layers thinner than 200 nm, while only a slight contrast is found for thicker layers.

3.2.2 Analysis in the LWIR range

In this section the study of the thermal hysteresis of the samples has been extended in the LWIR range (8-12 μm). Reflectance measurements *vs* temperature are shown in fig. 9, respectively for samples (a) S3 ($t_{VO_2} = 45$ nm), (b) S2 ($t_{VO_2} = 90$ nm) and (c) S1 ($t_{VO_2} = 135$ nm). Since transmittance through the 0.5 mm sapphire substrate is negligible in the LWIR range (T=0.001), emissivity has been calculated by using the formula $\varepsilon = 1 - R$; the results are shown in fig. 9(d-f). Reflectance in the LWIR range, similarly to SWIR range, switches from the low value around 0.07 at 30 °C when VO$_2$ behaves as a semiconductor (0.07 is also for the sapphire substrate) to much larger values at 90 °C when VO$_2$ is in the metallic state. The VO$_2$ films exhibit also an increasing reflectance with their thickness (see table 2). Moreover, a large
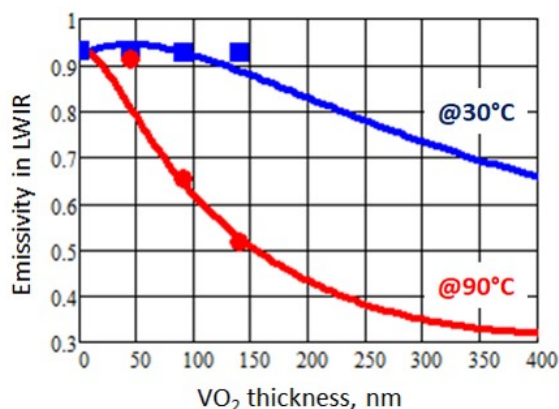

Fig. 10 Calculated emissivity in the LWIR range (8-2 μm) vs VO$_2$ film thickness. Red (blue) colors are for the metallic (semiconductor) phase. Symbols are for the experimental results of samples S1 (135 nm), S2 (90 nm) and S3 (45 nm) and the bare sapphire substrate. Continuous lines are for the numerical simulations.

negative differential thermal emissivity ($\varepsilon_H - \varepsilon_C < 0$) is observed, due mainly to the strong absorption of the sapphire substrate in the LWIR. This can be used for example for thermal camouflage: in this case thermal cameras working in the range 8-14 μm detect a cooler apparent temperature when the sample is heated up across the phase transition.[34]

In order to simulate the reflectance measurements, we used for the vanadium dioxide refractive index in the LWIR range the values reported in Ref.[35]: $n_C = 3.25 + 1.5i$ in the semiconductor

phase, and $n_H = 5 + 5i$ in the metallic phase; the value for the sapphire substrate was taken from Ref.[62]. The emissivity in the LWIR range of VO_2/sapphire structure *vs* VO_2 film thickness is shown in fig. 10. Numerical simulations (continuous lines) are in good agreement with the experimental measurements (symbols). Simulations confirm also that a large negative differential emissivity always occurs in the LWIR (see fig. 10), unlike the results obtained in the SWIR where a positive differential emissivity has been found (see fig.7c).

4   Conclusions

The hysteretic behavior of the SMT transition of VO_2 thin films of different thickness deposited by pulsed laser deposition on sapphire substrates has been investigated by combining *in-situ* structural and optical measurements. Reproducible hysteresis cycles exhibiting a width inversely proportional to the VO_2 crystallite size have been obtained. In general, the width of the transition upon heating is slightly sharper than the corresponding width during the cooling cycles, as explained in terms of the size distribution and of the different strain contribution in the two cycles. The main results indicate a good agreement between XRD and optical analysis, therefore demonstrating that the structural transition from monoclinic to tetragonal phases is the dominating mechanism for controlling the global properties of the SMT transition. Minor differences in the measured quantities (width of the hysteresis, absolute values of the transition temperatures upon heating and cooling,...) with the two employed characterization techniques can be ascribed to possible amorphous components embedded in the deposited films, which can act as defects in the structure, therefore influencing to a lesser extent the XRD measurements, which are sensitive to the crystalline component only, unlike the optical techniques in the IR spectral range, which are instead sensitive to the global, effective medium properties of the films. Although XRD results at the SMT can be consistently modeled with either a coexistence of the two phases or a continuous transition between the two, the optical results and in particular the *anomalous absorption* are better understood in terms of the first mechanism.

Conflicts of interest

There are no conflicts to declare.

Acknowledgements

References

1 D. N. Basov, R. D. Averitt and D. Hsieh, *Nature Materials*, 2017, **16**, 1077–1088.

2 S. V. Makarov, A. S. Zalogina, M. Tajik, D. A. Zuev, M. V. Rybin, A. A. Kuchmizhak, S. Juodkazis and Y. Kivshar, *Laser & Photonics Reviews*, 2017, **11**, 1700108.

3 P. Hosseini, C. D. Wright and H. Bhaskaran, *Nature*, 2014, **511**, 206–211.

4 K. J. Miller, R. F. Haglund and S. M. Weiss, *Optical Materials Express*, 2018, **8**, 2415–2429.

5 Z. Yang, C. Ko and S. Ramanathan, *Annual Review of Materials Research*, 2011, **41**, 337–367.

6 K. Liu, S. Lee, S. Yang, O. Delaire and J. Wu, *Materials Today*, 2018, **21**, 875–896.

7 Y. Ke, S. Wang, G. Liu, M. Li, T. J. White and Y. Long, *Small*, 2018, **14**, 1802025.

8 E. Petronijevic, M. Centini, T. Cesca, G. Mattei, F. A. Bovino and C. Sibilia, *Optics Express*, 2019, in press.

9 Z. Zhu, P. G. Evans, R. F. Haglund and J. G. Valentine, *Nano Letters*, 2017, **17**, 4881–4885.

10 T. Jostmeier, M. Mangold, J. Zimmer, H. Karl, H. J. Krenner, C. Ruppert and M. Betz, *Optics Express*, 2016, **24**, 17321–17331.

11 C. Wu, F. Feng and Y. Xie, *Chemical Society Reviews*, 2013, **42**, 5157–5183.

12 Y. Gao, H. Luo, Z. Zhang, L. Kang, Z. Chen, J. Du, M. Kanehira and C. Cao, *Nano Energy*, 2012, **1**, 221–246.

13 H. Coy, R. Cabrera, N. Sepúlveda and F. E. Fernández, *Journal of Applied Physics*, 2010, **108**, 113115.

14 F. J. Morin, *Physical Review Letters*, 1959, **3**, 34–36.

15 J. B. Goodenough, *Journal of Solid State Chemistry*, 1971, **3**, 490–500.

16 S. Lee, K. Hippalgaonkar, F. Yang, J. Hong, C. Ko, J. Suh, K. Liu, K. Wang, J. J. Urban, X. Zhang, C. Dames, S. A. Hartnoll, O. Delaire and J. Wu, *Science*, 2017, **355**, 371–374.

17 W.-T. Liu, J. Cao, W. Fan, Z. Hao, M. C. Martin, Y. R. Shen, J. Wu and F. Wang, *Nano Letters*, 2011, **11**, 466–470.

18 G. Leahu, R. Li Voti, C. Sibilia and M. Bertolotti, *Applied Physics Letters*, 2013, **103**, 231114.

19 R. Li Voti, G. L. Leahu, M. C. Larciprete, C. Sibilia and M. Bertolotti, *International Journal of Thermophysics*, 2015, **36**, 1004–1015.

20 M. Soltani, M. Chaker, E. Haddad, R. Kruzelecky, J. Margot, P. Laou and S. Paradis, *Journal of Vacuum Science & Technology A*, 2008, **26**, 763–767.

21 A. Pashkin, C. Kübler, H. Ehrke, R. Lopez, A. Halabica, R. F. Haglund, R. Huber and A. Leitenstorfer, *Physical Review B*, 2011, **83**, 195120.

22 V. R. Morrison, R. P. Chatelain, K. L. Tiwari, A. Hendaoui, A. Bruhács, M. Chaker and B. J. Siwick, *Science*, 2014, **346**, 445–448.

23 S. Wall, S. Yang, L. Vidas, M. Chollet, J. M. Glownia, M. Kozina, T. Katayama, T. Henighan, M. Jiang, T. A. Miller, D. A. Reis, L. A. Boatner, O. Delaire and M. Trigo, *Science*, 2018, **362**, 572–576.

24 S. Cueff, D. Li, Y. Zhou, F. J. Wong, J. A. Kurvits, S. Ramanathan and R. Zia, *Nature Communications*, 2015, **6**, 8636.

25 O. L. Muskens, L. Bergamini, Y. Wang, J. M. Gaskell, N. Zabala, C. de Groot, D. W. Sheel and J. Aizpurua, *Light: Science & Applications*, 2016, **5**, e16173–e16173.

26 E. B. Shadrin, A. V. Il'inskiǐ, A. I. Sidorov and S. D. Khanin, *Physics of the Solid State*, 2010, **52**, 2426–2433.

27 D. Brassard, S. Fourmaux, M. Jean-Jacques, J. C. Kieffer and M. A. El Khakani, *Applied Physics Letters*, 2005, **87**, 051910.

28 J. Y. Suh, R. Lopez, L. C. Feldman and R. F. Haglund, *Journal of Applied Physics*, 2004, **96**, 1209–1213.

29 R. Lopez, L. A. Boatner, T. E. Haynes, L. C. Feldman and R. F. Haglund, *Journal of Applied Physics*, 2002, **92**, 4031–4036.

30 F. Guinneton, L. Sauques, J.-C. Valmalette, F. Cros and J.-R. Gavarri, *Thin Solid Films*, 2004, **446**, 287–295.

31 J. Narayan and V. M. Bhosle, *Journal of Applied Physics*, 2006, **100**, 103524.

32 J. A. Ramirez-Rincon, C. L. Gomez-Heredia, A. Corvisier, J. Ordonez-Miranda, T. Girardeau, F. Paumier, C. Champeaux, F. Dumas-Bouchiat, Y. Ezzahri, K. Joulain, O. Ares and J. J. Alvarado-Gil, *Journal of Applied Physics*, 2018, **124**, 195102.

33 H. Prod'homme, J. Ordonez-Miranda, Y. Ezzahri, J. Drévillon and K. Joulain, *Journal of Quantitative Spectroscopy and Radiative Transfer*, 2018, **210**, 52–61.

34 M. A. Kats, R. Blanchard, S. Zhang, P. Genevet, C. Ko, S. Ramanathan and F. Capasso, *Physical Review X*, 2013, **3**, 041004.

35 M. A. Kats, D. Sharma, J. Lin, P. Genevet, R. Blanchard, Z. Yang, M. M. Qazilbash, D. N. Basov, S. Ramanathan and F. Capasso, *Applied Physics Letters*, 2012, **101**, 221101.

36 R. Li Voti, M. C. Larciprete, G. Leahu, C. Sibilia and M. Bertolotti, *Journal of Applied Physics*, 2012, **112**, 034305.

37 R. Li Voti, M. C. Larciprete, G. Leahu, C. Sibilia and M. Bertolotti, *Journal of Nanophotonics*, 2012, **6**, 061601.

38 G. Cesarini, G. L. Leahu, R. Li Voti, C. Sibilia and M. Bertolotti, *Proceedings SPIE, Metamaterials XI*, 2018, **10671**, 106711H.

39 G. Cesarini, G. Leahu, R. Li Voti and C. Sibilia, *Infrared Physics & Technology*, 2018, **93**, 112–115.

40 G. A. Nyberg and R. A. Buhrman, *Thin Solid Films*, 1987, **147**, 111–116.

41 G. A. Rozgonyi and D. H. Hensler, *Journal of Vacuum Science and Technology*, 1968, **5**, 194–199.

42 C. H. Griffiths and H. K. Eastwood, *Journal of Applied Physics*, 1974, **45**, 2201–2206.

43 E. E. Chain, *Journal of Vacuum Science & Technology A*, 1986, **4**, 432–435.

44 E. Kusano, J. A. Theil and J. A. Thornton, *Journal of Vacuum Science & Technology A*, 1988, **6**, 1663–1667.

45 H. K. Kim, H. You, R. P. Chiarello, H. L. M. Chang, T. J. Zhang and D. J. Lam, *Physical Review B*, 1993, **47**, 12900–12907.

46 C. M. Foster, R. P. Chiarello, H. L. M. Chang, H. You, T. J. Zhang, H. Frase, J. C. Parker and D. J. Lam, *Journal of Applied Physics*, 1993, **73**, 2841–2847.

47 Y. Dachuan, X. Niankan, Z. Jingyu and Z. Xiulin, *Journal of Physics D: Applied Physics*, 1996, **29**, 1051–1057.

48 R. K. Singh and J. Narayan, *Journal of Applied Physics*, 1990, **67**, 3785–3790.

49 C. L. Gomez-Heredia, J. A. Ramirez-Rincon, J. Ordonez-Miranda, O. Ares, J. J. Alvarado-Gil, C. Champeaux, F. Dumas-Bouchiat, Y. Ezzahri and K. Joulain, *Scientific Reports*, 2018, **8**, 8479.

50 T. Yao, X. Zhang, Z. Sun, S. Liu, Y. Huang, Y. Xie, C. Wu, X. Yuan, W. Zhang, Z. Wu, G. Pan, F. Hu, L. Wu, Q. Liu and S. Wei, *Physical Review Letters*, 2010, **105**, 226405.

51 J. Nag and R. F. H. Jr, *Journal of Physics: Condensed Matter*, 2008, **20**, 264016.

52 M. Mosca, R. Macaluso, C. Calì, R. Butté, S. Nicolay, E. Feltin, D. Martin and N. Grandjean, *Thin Solid Films*, 2013, **539**, 55–59.

53 A. Boughelout, R. Macaluso, I. Crupi, B. Megna, M. S. Aida and M. Kechouane, *Journal of Electronic Materials*, 2019, **48**, 4381–4388.

54 L. Lutterotti, *Nuclear Instruments and Methods in Physics Research Section B: Beam Interactions with Materials and Atoms*, 2010, **268**, 334–340.

55 H. Bialas, A. Dillenz, H. Downar and P. Ziemann, *Thin Solid Films*, 1999, **338**, 60–69.

56 M. Nazari, Y. Zhao, V. V. Kuryatkov, Z. Y. Fan, A. A. Bernussi and M. Holtz, *Physical Review B*, 2013, **87**, 035142.

57 V. Théry, A. Boulle, A. Crunteanu, J. C. Orlianges, A. Beaumont, R. Mayet, A. Mennai, F. Cosset, A. Bessaudou and M. Fabert, *Physical Review B*, 2016, **93**, 184106.

58 T.-H. Yang, R. Aggarwal, A. Gupta, H. Zhou, R. J. Narayan and J. Narayan, *Journal of Applied Physics*, 2010, **107**, 053514.

59 V. A. Klimov, I. O. Timofeeva, S. D. Khanin, E. B. Shadrin, A. V. Ilinskii and F. Silva-Andrade, *Technical Physics*, 2002, **47**, 1134–1139.

60 R. Lopez, T. E. Haynes, L. A. Boatner, L. C. Feldman and R. F. Haglund, *Physical Review B*, 2002, **65**, 224113.

61 M. M. Qazilbash, M. Brehm, B.-G. Chae, P.-C. Ho, G. O. Andreev, B.-J. Kim, S. J. Yun, A. V. Balatsky, M. B. Maple, F. Keilmann, H.-T. Kim and D. N. Basov, *Science*, 2007, **318**, 1750–1753.

62 J. Kischkat, S. Peters, B. Gruska, M. Semtsiv, M. Chashnikova, M. Klinkmüller, O. Fedosenko, S. Machulik, A. Aleksandrova, G. Monastyrskyi, Y. Flores and W. T. Masselink, *Appl. Opt.*, 2012, **51**, 6789–6798.

63 K. Shibuya and A. Sawa, *AIP Advances*, 2015, **5**, 107118.

64 E. E. Chain, *Applied Optics*, 1991, **30**, 2782–2787.

65 O. P. Konovalova, A. I. Sidorov and I. I. Shaganov, *Journal of Optical Technology*, 1999, **66**, 391.

66 H. Kakiuchida, P. Jin, S. Nakao and M. Tazawa, *Japanese Journal of Applied Physics*, 2007, **46**, L113.

67 H. Kakiuchida, P. Jin and M. Tazawa, *Solar Energy Materials and Solar Cells*, 2008, **92**, 1279–1284.

68 M. Tazawa, P. Jin and S. Tanemura, *Applied Optics*, 1998, **37**, 1858–1861.

69 F. Y. Gan and P. Laou, *Journal of Vacuum Science & Technology A*, 2004, **22**, 879–882.

70 G. Leahu, R. Li Voti, C. Sibilia, M. Bertolotti, V. Golubev and D. A. Kurdyukov, *Optical and Quantum Electronics*, 2007, **39**, 305–310.

71 S. Paradis, P. Mérel, P. Laou and D. Alain, *Proceeding SPIE, Photonics North*, 2006, **6343**, 63433U.